## Chapter 3.49

# Experimental arrangements for inelastic X-ray scattering spectroscopy

## Pieter Glatzel[a]* and Giacomo Ghiringhelli[b]

[a]ESRF – The European Synchrotron, 71 Avenue des Martyrs, 38000 Grenoble, France, and [b]Dipartimento di Fisica, Politecnico di Milano, Piazza Leonardo da Vinci 32, 20133 Milano, Italy. *Correspondence e-mail: glatzel@esrf.fr

Geometries for scanning and dispersive instruments for the spectroscopy of scattered X-rays are presented and the contributions to the energy bandwidth are discussed. Differences between hard and soft X-ray spectrometers are addressed.

## 1. Introduction

An instrument for analyzing the fine structure of the scattered X-rays in core-hole spectroscopy (X-ray emission spectroscopy, resonant inelastic X-ray scattering, X-ray Raman scattering *etc.*) requires an energy bandwidth that is of the order of the core-hole lifetime broadening. An energy bandwidth well below 10 eV is beyond the capabilities of semiconductor detectors, but can be achieved using wavelength-dispersive X-ray optics (Sa, 2014; Schülke, 2007). Instruments have been installed on many beamlines at storage rings and in laboratories (Zimmermann *et al.*, 2020). Solid-state detectors using superconducting materials are also able to reach an energy bandwidth of a few electronvolts (Uhlig *et al.*, 2015; Kurakado & Taniguchi, 2016; Doriese *et al.*, 2017; Li *et al.*, 2018). The widespread use of this technology for X-ray spectroscopy at storage rings has been hampered by the limited count rates that they can accept. For measurements where a few electronvolts suffice, the photon flux at synchrotron-radiation sources is often higher than can be handled by such detectors. Furthermore, the low temperatures of the detector material require sophisticated instrumentation. This technology is very promising and is currently finding many interesting applications at laboratory sources. This section focuses on wavelength-dispersive setups. We note that the field of inelastic X-ray scattering (IXS) traditionally also covers nuclear forward scattering and Compton scattering, which we do not discuss here.

Two important parameters characterize an X-ray spectrometer: the captured solid angle and the energy bandwidth that is given by the deviation $\delta\theta$,

$$\delta E = E\delta\theta \cot\theta. \tag{1}$$

The contributions to $\delta\theta$ are geometric and intrinsic. Geometric contributions consider the spectrometer geometry for a point source, contributions from a finite source size and, if relevant, the detector position resolution. Deviations of the reflecting surface from the theoretical shape also contribute to the broadening. Intrinsic contributions arise from the scattering properties of the optical element, which for crystal optics are evaluated using the theory of dynamical diffraction.

Energy analysis of the scattered X-rays can be achieved in a scanning or a dispersive setup (Fig. 1). Some instruments employ a combination of both (Huotari *et al.*, 2005). A scanning setup adopts a point-to-point focusing scheme where the optical element reflects all X-rays impinging on its surface within an angular range $\delta\theta$ onto a detector element. Alternatively, the X-rays may be dispersed by the optical element corresponding to their wavelengths onto a detector surface (typically a few cm$^2$), the position resolution of which allows X-rays with different wavelengths to be distinguished. A dispersive setup does not require moving parts during the acquisition of a spectrum and accumulation is performed for all energies simultaneously. Consequently, the spectrum does not necessarily have to be normalized to the incoming flux. Such a setup is mechanically less demanding and is compatible with single-shot data collection at, for example, free-electron lasers. A scanning setup combines the entire solid angle captured by the crystal surface in one energy (within $\delta E$) and

the X-rays are focused on a single-element or multi-element detector. The required detector surface is governed by the focal spot size, which is typically a few mm$^2$. A small exposed detector surface minimizes the background from stray X-rays. A scanning setup is preferable for high energy resolution fluorescence detection X-ray absorption spectroscopy (HERFD-XAS) and often for measurements on dilute samples. Scanning and dispersive spectrometers can be realized adopting different geometries and the most appropriate spectrometer geometry depends on the application. Another scheme is echo spectrometry, in which a polychromatic beam interacts with the sample and is imaged on a position-resolving detector (Shvyd'ko, 2017).

An important observation for inelastic scattering is that similar final, excited states (see Glatzel *et al.*, 2024) are observed in the soft and the hard X-ray range. The required energy bandwidth $\Delta E$ is thus the same and the energy resolving power $E/\Delta E$ must be considerably higher in the hard X-ray range, which can be achieved using perfect crystal Bragg optics, while gratings are used in the soft X-ray range.
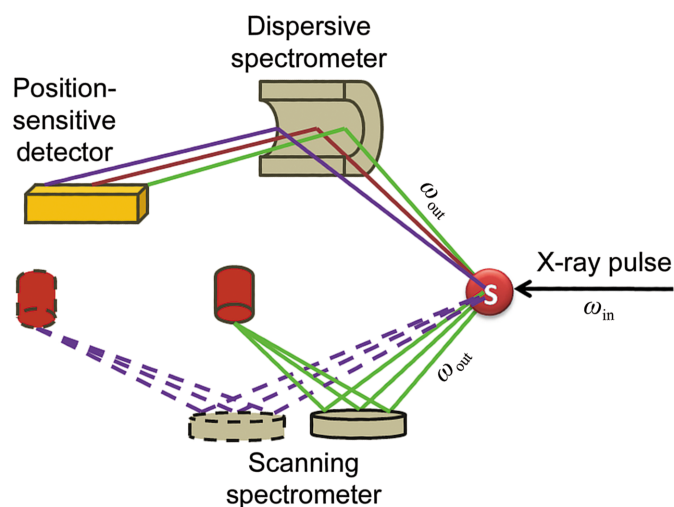


**Figure 1**
Scanning and dispersive setups for X-ray scattering spectroscopy.

## 2. Rowland circle

Henry August Rowland (1848–1901) conceived an optical scheme in which one optical element selects a wavelength and focuses light onto a detector. The Rowland circle is now ubiquitous on X-ray beamlines in the soft, tender and hard X-ray ranges. The principle is shown in Fig. 2. A divergent beam, *i.e.* the scattered X-rays, emerges from the source and illuminates the surface of the optical element on the Rowland circle. The radius of the circle is $R/2$. One now distinguishes between the surface of the optical element and the orientation of the reflecting crystal planes. The normal on the reflecting planes must intersect the Rowland circle at the central point $C$ in order to obtain the same Bragg angle across the whole surface in the Rowland plane. Consequently, the reflecting plane is parallel to the tangent to the Rowland circle only for
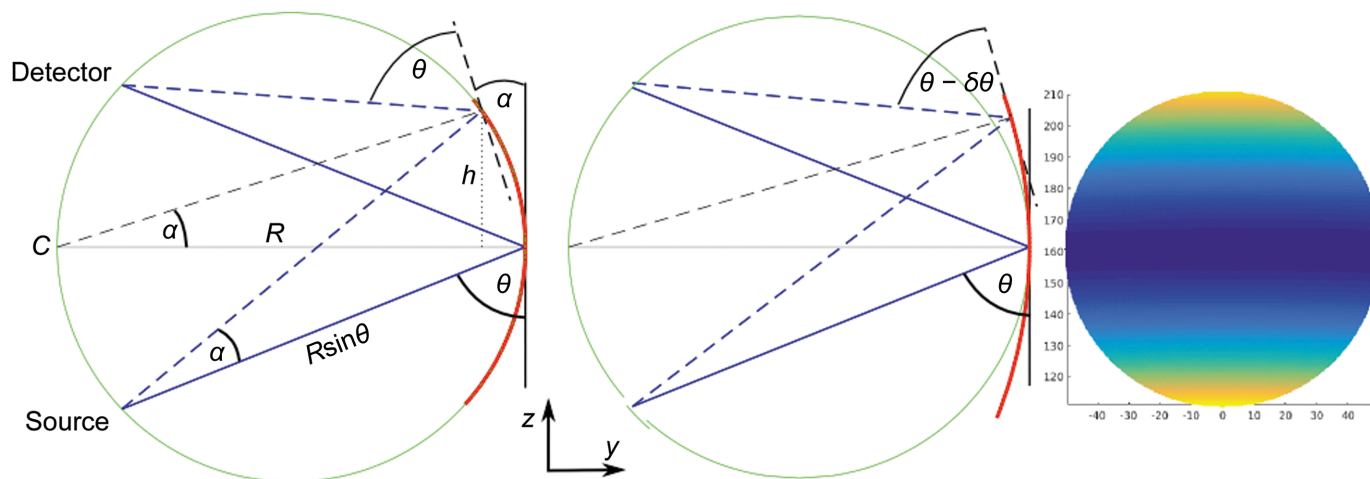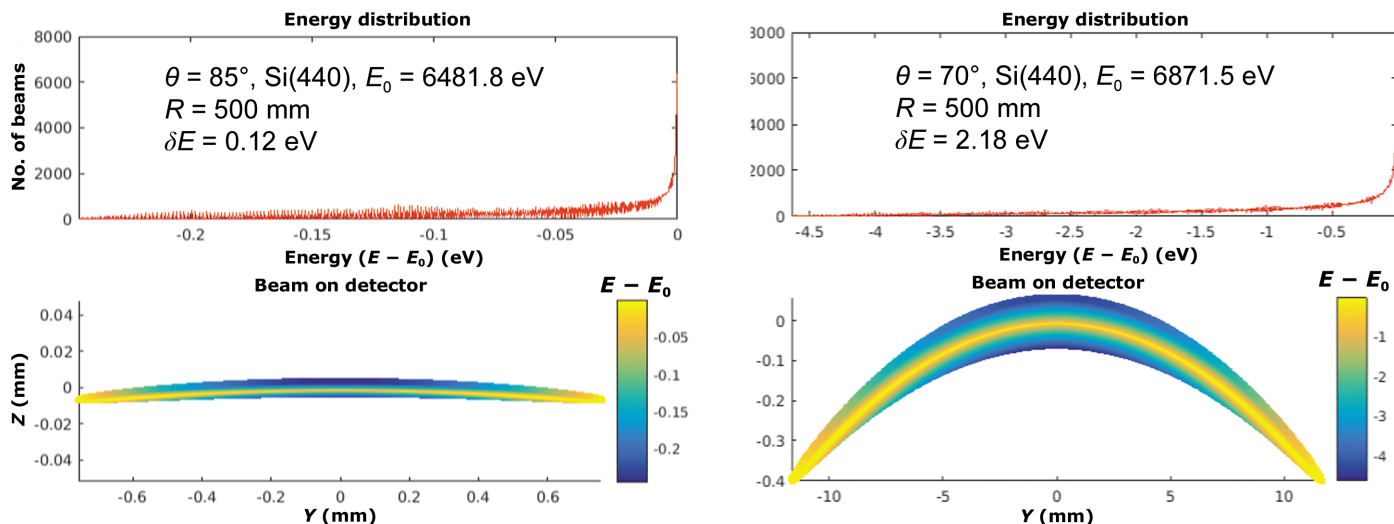


**Figure 2**
Rowland circle (green), surface of the optical element (red), light rays (blue) and orientation of reflecting crystal planes (black). Johansson (left) and Johann (middle) optical elements are shown. The panel on the right shows an example for a spherical ($R = 500$ mm) Johann crystal with a diameter of 100 mm. The colours indicate the Bragg angle.

**Figure 3**
Ray-tracing results for Johann geometry. Only geometric contributions are considered. The energy bandwidth was obtained from the histogram (top panels) including 80% of all rays. The bottom panels show the beam on the detector on the Rowland circle. Note the scale and aspect ratio of the axes. A full consideration of the energy bandwidth also includes the intrinsic contributions of a bent crystal (Honkanen *et al.*, 2014).

the beam in the centre of the optical element (opposite to point C). Above and below this central point, an angle $\alpha$ opens between the tangent on the Rowland circle (and thus the surface of the optical element) and the reflecting plane (which becomes a secant). This asymmetry angle depends on the displacement $h$ from the centre, and the radius of the X-ray-reflecting crystal plane is $R$. Such an optical element achieves exact meridional focusing in the detector on the Rowland circle (Johansson, 1933).

Fabrication of an optical element with a varying asymmetry angle, a Johansson crystal, is possible but challenging and thus expensive. A simpler setup without an asymmetry angle in the optical element is the Johann geometry (Johann, 1931), in which the surface of the optical element adopts a bending radius $R$ (Fig. 2, centre). This introduces a deviation $\delta\theta \simeq \frac{1}{2}E(z/R)^2\cot^2\theta$ of the reflection angle at a distance $z$ above and below the central line. This Johann error is the dominant geometrical contribution to the energy broadening for a point source. Another contribution arises from the optical element extending in the sagittal direction, *i.e.* perpendicular to the Rowland circle. This contribution to the energy bandwidth scales with $\cot(\theta)^4$ and can be neglected compared with other contributions (Fig. 2, right).

The geometric contributions due to the finite source sizes $S_z$ and $S_y$ are (Bergmann & Cramer, 1998)

$$\Delta E_z \simeq E\frac{S_z}{R}\cot\theta, \quad \Delta E_y \simeq \frac{S_y}{R}\cot^2\theta. \tag{2}$$

The contribution of the source size in the sagittal direction scales with $(S_x/R)^2$ and can be neglected for common beam shapes. The beam size should thus be minimized in the dispersive direction, while a larger beam can be tolerated in the other dimensions. Such considerations are important, for example, in the case of radiation-sensitive samples, where the incoming beam photon density should be minimized without losing energy resolution in the X-ray spectrometer.

Following the equations for a toroidal mirror (the first-order terms) the sagittal bending should be $R\sin^2\theta$ to achieve focusing at the detector position, *i.e.* the sagittal radius depends on the Bragg angle. Toroidal crystals with dynamical bending are demanding to fabricate. A spherical Johann crystal with fixed radius $R$ sagitally focuses at a distance $R\sin(-\theta)/\cos(2\theta)$ from the crystal surface compared with $R\sin\theta$ in the meridional direction.[1] The focus on a detector placed on the Rowland circle is in this case a line (in the $x$ direction) that becomes longer with decreasing Bragg angle. The sagittal and meridional focusing properties of the Rowland geometry close to backscattering have been used by Huotari and coworkers for imaging applications using X-ray Raman scattering (Huotari *et al.*, 2011). We note that cylindrical crystals can be used with the bending radius in the sagittal or the meridional plane.

The construction of an instrument for X-ray scattering spectroscopy requires a careful analysis of all contributions to the energy broadening and focal spot size. Analytical formulae have been derived by various authors that provide insight into important contributions to the broadening (Suortti *et al.*, 1999; Bergmann & Cramer, 1998). The errors scale with $\cot(\theta)^n$, *i.e.* increase with decreasing Bragg angle, and many instruments in the hard X-ray range use analyzer crystals with a spherical shape at Bragg angles higher than 70° (Fig. 3). A direct consequence is that many different crystal reflections and crystal materials (for example silicon, germanium, $LiNbO_3$ and $SiO_2$) are required in order to cover the fluorescence lines of different elements. Instruments for nonresonant inelastic X-ray scattering with very high resolving power work very close to backscattering (Sinn *et al.*, 2001; Krisch & Sette, 2017).

The bending radius should be minimized in order to capture a large solid angle. This is limited by the elasticity of the wafer,

---

[1] The Johann error also introduces a small, meridional broadening of the focus. This error corresponds to the higher order terms of the focusing equations for a toroidal mirror.

which will break when bent too much. The bending furthermore introduces an elastic stress that degrades the intrinsic resolution (Honkanen *et al.*, 2014; Masciovecchio *et al.*, 1996). Crystal analyzers with very thin wafers and/or wafer segmentation allow smaller bending radii (Szlachetko *et al.*, 2012; Mattern *et al.*, 2012; Rovezzi *et al.*, 2017; Dickinson *et al.*, 2008). A related consideration concerns the required space around the sample. The detector moves closer to the sample with increasing Bragg angle and decreasing bending radius (Fig. 2). Sample environments such as cryostats and *in situ* cells require a minimum of space, which in turn sets an upper limit for the Bragg angle at a given radius of the Rowland circle.

## 3. Dispersive geometries

A continuous variation of the Bragg angle across the surface of an optical element in combination with a position-sensitive detector allows the detection of an extended energy range simultaneously, *i.e.* without the need to move the elements of the spectrometer. Giving up the Rowland condition by moving the source in or out of the Rowland circle results in a dispersive geometry (Machek *et al.*, 2007; Kavčič *et al.*, 2012; Abraham *et al.*, 2019). A commonly used dispersive geometry is the von Hámos geometry, in which the meridional radius is infinite and the sagittal radius is $R$, *i.e.* the crystal is cylindrical (Gouy, 1916; Hámos, 1932). The dispersion is given by $X = 2R\cot\theta$, where the distance $X$ is between the source point on the cylindrical axis and the image point (Shevelko *et al.*, 2002). $R$ is the cylinder radius. The dispersive energy range for a given central Bragg angle is determined by the cylinder length, radius and crystal reflection (Sahle *et al.*, 2023). The dispersive geometry allows the use of mosaic crystals (Anklamm *et al.*, 2014). Sagittal focusing is achieved at a distance $R/\sin\theta$ between the source/detector and the crystal surface. The finite source size and intrinsic broadening $\delta\theta$ of the optical element result in an *x*-shaped focus (Zastrau *et al.*, 2012).

Single-element, 1D and 2D detectors may be used in an X-ray spectrometer. The count rates may vary between megahertz (for example the $K\alpha$ lines of $3d$ transition metals) and a few hertz or even less (for example phonons and magnons) and the requirements with respect to dynamic range and dark counts are very strict. High energy resolution fluorescence detection X-ray absorption spectroscopy/partial fluorescence yield X-ray absorption near-edge structure (HERFD/PFY-XANES) is often carried out in continuous (on-the-fly) acquisition mode and the beamline electronics should be capable of counting times in the millisecond range. Energy resolution may also be required in the photon detector (for example silicon drift diode detectors) for highly dilute samples and/or samples in a complex matrix where photons from unwanted fluorescence lines or X-ray scattering events reach the detector with count rates similar to the desired photons. Lower order contributions [for example the (440) reflection when interested in the (660) reflection] can also be excluded. Position-sensitive detectors are mandatory for dispersive spectrometer geometries. A 1D detector is in principle sufficient for a von Hámos instrument, but 2D detectors are often used in order to facilitate alignment and provide flexibility for choosing the active detector area in the sagittal direction. Scanning spectrometers may also use the detector position resolution to improve the energy resolution (Huotari *et al.*, 2005).

## 4. Multi-analyzer spectrometers

It is desirable to increase the captured solid angle. A larger crystal diameter increases the energy bandwidth in Rowland geometry. A von Hámos geometry is exact in the sagittal direction, *i.e.* there is no contribution to $\delta\theta$, but extending the crystal in the meridional direction will only increase the energy range and not the captured solid angle per unit energy. Thus, in both geometries the solid angle is commonly increased by mounting several analyzer crystals where each crystal reflects at the same energy (Fig. 4). The main challenge
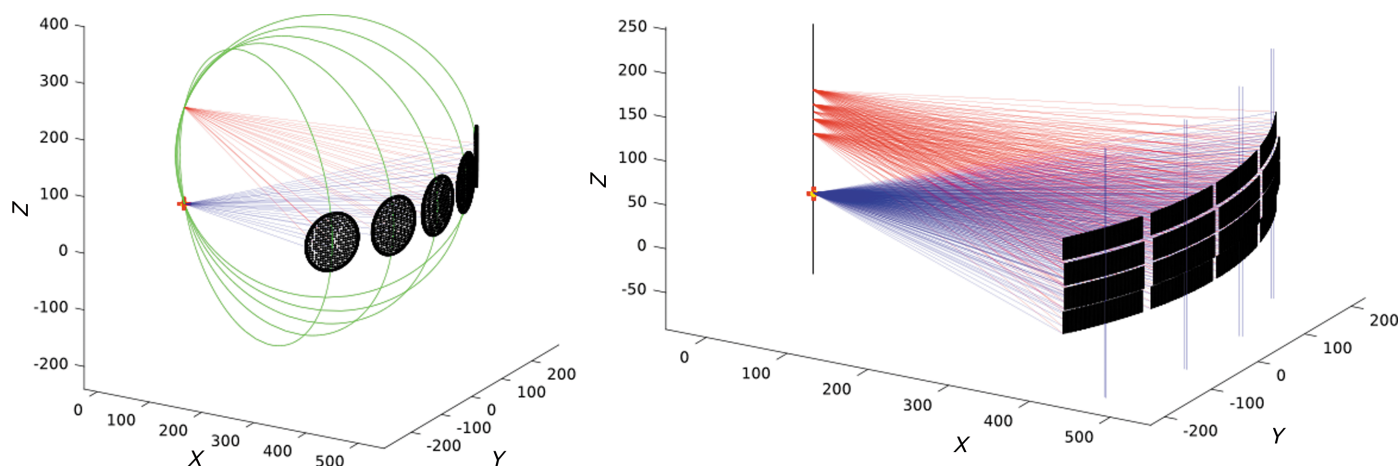


**Figure 4**
Multi-analyzer spectrometers in Rowland (left) and von Hámos (right) geometry. The Rowland circles are indicated in green and the X-ray source is indicated by a red cross. The crystal bending radius is 500 mm in both geometries.
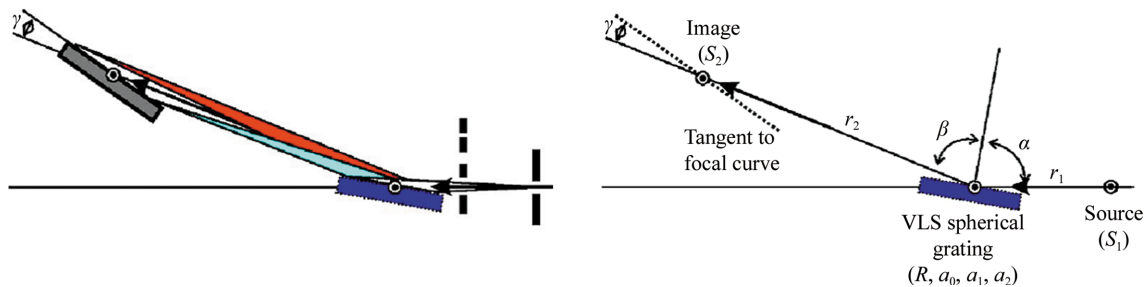
**Figure 5**
The concept of a soft X-ray spectrometer based on a grazing-incidence grating: radiation is dispersed in the tangential plane and is collected by a 2D detector at nearly grazing incidence. The angles and distances are defined in the sketch on the right.

here is to achieve an identical energy bandwidth and energy calibration for all crystals. Each crystal may reflect on the same or separate X-ray detectors and the detectors may be single-element or spatially resolving (Sokaras *et al.*, 2012, 2013; Huotari *et al.*, 2017; Hayashi *et al.*, 2004; Fister *et al.*, 2006; Alonso-Mori *et al.*, 2012; Kleymenov *et al.*, 2011; Dickinson *et al.*, 2008; Glatzel *et al.*, 2021; Moretti Sala *et al.*, 2018; Rovezzi *et al.*, 2020).

## 5. Soft X-ray spectrometers

For photon energies smaller than 1.5 keV, Bragg reflections from crystalline planes cannot be used to build narrow bandpass filters or dispersive optical elements because the lattice spacings of inorganic materials (resistant to beam damage) are too small with respect to the photon wavelength. Moreover, the penetration depth is strongly reduced by absorption, limiting the intrinsic resolution. Consequently, spectrometers for soft X-rays are based on gratings ruled on the surface of high-quality mirrors, mounted at very grazing incidence ($\sim$1.5–3° from the surface) to preserve reflectivity (Ghiringhelli *et al.*, 2006; Harada *et al.*, 2012; Dvorak *et al.*, 2016). The dispersion properties are described by the grating equation

$$E = K \frac{na}{\sin \alpha - \sin \beta}, \tag{3}$$

where the photon energy $E$ is measured in electronvolts, $n$ is the diffraction order (usually $+1$), $a$ is the groove density (in $\text{mm}^{-1}$), $K = 1.239842 \times 10^{-3}$ eV mm and the angles are defined in Fig. 5. The focusing properties of the grating are provided by the curvature of its surface (usually a sphere with radius $R$), by a nonconstant $a$ along the tangential direction (variable line-spacing grating) or by a combination of the two. In the former case a Rowland circle mounting is usually adopted. In the latter cases the linear term $a_1$ in the groove-density polynomial law [$a(x) = a_0 + a_1 x + a_2 x^2 + \dots$] intervenes in the focusing equation

$$\frac{\cos^2 \alpha}{r_1} + \frac{\cos^2 \beta}{r_2} = \frac{\cos \alpha + \cos \beta}{R} + K \frac{na_1}{E}. \tag{4}$$

The quadratic term $a_2$ can be used to minimize optical aberrations.

One grating can cover a wide energy range provided that the detector can be moved along the focal line. The detector is usually 2D and is preferably mounted tangentially to the focal line. The energy bandwidth of the system has three main contributions that add quadratically: the source size in the dispersion direction ($S_1$), the detector spatial resolution ($S_2$) and the surface slope error of the grating. The first two contributions ($\Delta E_1$ and $\Delta E_2$) decrease when the optical arms ($r_1$ is the sample-to-grating distance and $r_2$ is the grating-to-detector distances) are made longer, so high-resolution spectrometers are usually several metres long (Zhou *et al.*, 2022; Schulz *et al.*, 2020; Brookes *et al.*, 2018). The progress in beamline optics, leading to a smaller spot size on the sample and to a lower slope-error contribution, and in X-ray detector technology, allowing better spatial resolution, in particular with the use of single-photon detection (Amorese *et al.*, 2019), has led to constant improvements in instrumental bandwidth. The angular acceptance of soft X-ray spectrometers is relatively small and is limited to $\sim$3 mrad in the dispersive direction by optical aberrations and in the nondispersive directions to $\sim$20–30 mrad by the detector size (in the absence of additional optical elements).

Spectra are measured at a fixed position of the detector, acquiring an energy window of several electronvolts in parallel. One resonant inelastic X-ray scattering spectrum can take from a few minutes to several hours of accumulation time, depending on the energy resolution and specific cross sections. The resolution can be as good as 20 meV around 1 keV for 10 m spectrometers.

## References

Abraham, B., Nowak, S., Weninger, C., Armenta, R., Defever, J., Day, D., Carini, G., Nakahara, K., Gallo, A., Nelson, S., Nordlund, D., Kroll, T., Hunter, M. S., van Driel, T., Zhu, D., Weng, T.-C., Alonso-Mori, R. & Sokaras, D. (2019). *J. Synchrotron Rad.* **26**, 629–634.
Alonso-Mori, R., Kern, J., Sokaras, D., Weng, T.-C., Nordlund, D., Tran, R., Montanez, P., Delor, J., Yachandra, V. K., Yano, J. & Bergmann, U. (2012). *Rev. Sci. Instrum.* **83**, 073114.
Amorese, A., Langini, C., Dellea, G., Kummer, K., Brookes, N. B., Braicovich, L. & Ghiringhelli, G. (2019). *Nucl. Instrum. Methods Phys. Res. A*, **935**, 227–231.
Anklamm, L., Schlesiger, C., Malzer, W., Grötzsch, D., Neitzel, M. & Kanngiesser, B. (2014). *Rev. Sci. Instrum.* **85**, 053110.
Bergmann, U. & Cramer, S. P. (1998). *Proc. SPIE*, **3448**, 198.
Brookes, N. B., Yakhou-Harris, F., Kummer, K., Fondacaro, A., Cezar, J. C., Betto, D., Velez-Fort, E., Amorese, A., Ghiringhelli, G.,

Braicovich, L., Barrett, R., Berruyer, G., Cianciosi, F., Eybert, L., Marion, P., van der Linden, P. & Zhang, L. (2018). *Nucl. Instrum. Methods Phys. Res. A*, **903**, 175–192.

Dickinson, B., Seidler, G. T., Webb, Z. W., Bradley, J. A., Nagle, K. P., Heald, S. M., Gordon, R. A. & Chou, I. M. (2008). *Rev. Sci. Instrum.* **79**, 123112.

Doriese, W. B., Abbamonte, P., Alpert, B. K., Bennett, D. A., Denison, E. V., Fang, Y., Fischer, D. A., Fitzgerald, C. P., Fowler, J. W., Gard, J. D., Hays-Wehle, J. P., Hilton, G. C., Jaye, C., McChesney, J. L., Miaja-Avila, L., Morgan, K. M., Joe, Y. I., O'Neil, G. C., Reintsema, C. D., Rodolakis, F., Schmidt, D. R., Tatsuno, H., Uhlig, J., Vale, L. R., Ullom, J. N. & Swetz, D. S. (2017). *Rev. Sci. Instrum.* **88**, 053108.

Dvorak, J., Jarrige, I., Bisogni, V., Coburn, S. & Leonhardt, W. (2016). *Rev. Sci. Instrum.* **87**, 115109.

Fister, T. T., Seidler, G. T., Wharton, L., Battle, A. R., Ellis, T. B., Cross, J. O., Macrander, A. T., Elam, W. T., Tyson, T. A. & Qian, Q. (2006). *Rev. Sci. Instrum.* **77**, 063901.

Ghiringhelli, G., Piazzalunga, A., Dallera, C., Trezzi, G., Braicovich, L., Schmitt, T., Strocov, V. N., Betemps, R., Patthey, L., Wang, X. & Grioni, M. (2006). *Rev. Sci. Instrum.* **77**, 113108.

Glatzel, P., Harris, A., Marion, P., Sikora, M., Weng, T.-C., Guilloud, C., Lafuerza, S., Rovezzi, M., Detlefs, B. & Ducotté, L. (2021). *J. Synchrotron Rad.* **28**, 362–371.

Glatzel, P., Juhin, A. & Moretti, M. (2024). *Int. Tables Crystallogr. I*, ch. 2.19, 177–189.

Gouy, M. (1916). *Ann. Phys.* **9**, 241–248.

Hámos, L. von (1932). *Naturwissenschaften*, **20**, 705–706

Harada, Y., Kobayashi, M., Niwa, H., Senba, Y., Ohashi, H., Tokushima, T., Horikawa, Y., Shin, S. & Oshima, M. (2012). *Rev. Sci. Instrum.* **83**, 013116.

Hayashi, H., Kawata, M., Takeda, R., Udagawa, Y., Watanabe, Y., Takano, T., Nanao, S. & Kawamura, N. (2004). *J. Electron Spectrosc. Relat. Phenom.* **136**, 191–197.

Honkanen, A.-P., Verbeni, R., Simonelli, L., Moretti Sala, M., Monaco, G. & Huotari, S. (2014). *J. Synchrotron Rad.* **21**, 104–110.

Huotari, S., Pylkkänen, T., Verbeni, R., Monaco, G. & Hämäläinen, K. (2011). *Nat. Mater.* **10**, 489–493.

Huotari, S., Sahle, C. J., Henriquet, C., Al-Zein, A., Martel, K., Simonelli, L., Verbeni, R., Gonzalez, H., Lagier, M.-C., Ponchut, C., Moretti Sala, M., Krisch, M. & Monaco, G. (2017). *J. Synchrotron Rad.* **24**, 521–530.

Huotari, S., Vankó, G., Albergamo, F., Ponchut, C., Graafsma, H., Henriquet, C., Verbeni, R. & Monaco, G. (2005). *J. Synchrotron Rad.* **12**, 467–472.

Johann, H. H. (1931). *Z. Phys.* **69**, 185–206.

Johansson, T. (1933). *Z. Phys.* **82**, 507–528.

Kavčič, M., Budnar, M., Mühleisen, A., Gasser, F., Žitnik, M., Bučar, K. & Bohinc, R. (2012). *Rev. Sci. Instrum.* **83**, 033113.

Kleymenov, E., van Bokhoven, J. A., David, C., Glatzel, P., Janousch, M., Alonso-Mori, R., Studer, M., Willimann, M., Bergamaschi, A., Henrich, B. & Nachtegaal, M. (2011). *Rev. Sci. Instrum.* **82**, 065107.

Krisch, M. & Sette, F. (2017). *Crystallogr. Rep.* **62**, 1–12.

Kurakado, M. & Taniguchi, K. (2016). *J. Instrum.* **11**, C12071.

Li, D., Alpert, B. K., Becker, D. T., Bennett, D. A., Carini, G. A., Cho, H. M., Doriese, W. B., Dusatko, J. E., Fowler, J. W., Frisch, J. C., Gard, J. D., Guillet, S., Hilton, G. C., Holmes, M. R., Irwin, K. D., Kotsubo, V., Lee, S. J., Mates, J. A. B., Morgan, K. M., Nakahara, K., Pappas, C. G., Reintsema, C. D., Schmidt, D. R., Smith, S. R., Swetz, D. S., Thayer, J. B., Titus, C. J., Ullom, J. N., Vale, L. R., Van Winkle, D. D., Wessels, A. & Zhang, L. (2018). *J. Low Temp. Phys.* **193**, 1287–1297.

Machek, P., Welter, E., Caliebe, W., Brüggmann, U., Dräger, G. & Fröba, M. (2007). *AIP Conf. Proc.* **879**, 1755–1758.

Masciovecchio, C., Bergmann, U., Krisch, M., Ruocco, G., Sette, F. & Verbeni, R. (1996). *Nucl. Instrum. Methods Phys. Res. B*, **111**, 181–186.

Mattern, B. A., Seidler, G. T., Haave, M., Pacold, J. I., Gordon, R. A., Planillo, J., Quintana, J. & Rusthoven, B. (2012). *Rev. Sci. Instrum.* **83**, 023901.

Moretti Sala, M., Martel, K., Henriquet, C., Al Zein, A., Simonelli, L., Sahle, C., Gonzalez, H., Lagier, M.-C., Ponchut, C., Huotari, S., Verbeni, R., Krisch, M. & Monaco, G. (2018). *J. Synchrotron Rad.* **25**, 580–591.

Rovezzi, M., Harris, A., Detlefs, B., Bohdan, T., Svyazhin, A., Santambrogio, A., Degler, D., Baran, R., Reynier, B., Noguera Crespo, P., Heyman, C., Van Der Kleij, H.-P., Van Vaerenbergh, P., Marion, P., Vitoux, H., Lapras, C., Verbeni, R., Kocsis, M. M., Manceau, A. & Glatzel, P. (2020). *J. Synchrotron Rad.* **27**, 813–826.

Rovezzi, M., Lapras, C., Manceau, A., Glatzel, P. & Verbeni, R. (2017). *Rev. Sci. Instrum.* **88**, 013108.

Sa, J. (2014). *High-Resolution XAS/XES: Analyzing Electronic Structures of Catalysts*. Boca Raton: CRC Press.

Sahle, C. J., Gerbon, F., Henriquet, C., Verbeni, R., Detlefs, B., Longo, A., Mirone, A., Lagier, M.-C., Otte, F., Spiekermann, G. & Petit-girard, S. (2023). *J. Synchrotron Rad.* **30**, 251–257.

Schülke, W. (2007). *Electron Dynamics by Inelastic X-ray Scattering*. Oxford University Press.

Schulz, C., Lieutenant, K., Xiao, J., Hofmann, T., Wong, D. & Habicht, K. (2020). *J. Synchrotron Rad.* **27**, 238–249.

Shevelko, A. P., Kasyanov, Y. S., Yakushev, O. F. & Knight, L. V. (2002). *Rev. Sci. Instrum.* **73**, 3458–3463.

Shvyd'ko, Y. (2017). *arXiv*:1704.01239.

Sinn, H., Alp, E. E., Alatas, A., Barraza, J., Bortel, G., Burkel, E., Shu, D., Sturhahn, W., Sutter, J. P., Toellner, T. S. & Zhao, J. (2001). *Nucl. Instrum. Methods Phys. Res. A*, **467–468**, 1545–1548.

Sokaras, D., Nordlund, D., Weng, T., Mori, R. A., Velikov, P., Wenger, D., Garachtchenko, A., George, M., Borzenets, V., Johnson, B., Qian, Q., Rabedeau, T. & Bergmann, U. (2012). *Rev. Sci. Instrum.* **83**, 043112.

Sokaras, D., Weng, T. C., Nordlund, D., Alonso-Mori, R., Velikov, P., Wenger, D., Garachtchenko, A., George, M., Borzenets, V., Johnson, B., Rabedeau, T. & Bergmann, U. (2013). *Rev. Sci. Instrum.* **84**, 053102.

Suortti, P., Buslaps, T., Fajardo, P., Honkimäki, V., Kretzschmer, M., Lienert, U., McCarthy, J. E., Renier, M., Shukla, A., Tschentscher, T. & Meinander, T. (1999). *J. Synchrotron Rad.* **6**, 69–80.

Szlachetko, J., Nachtegaal, M., de Boni, E., Willimann, M., Safonova, O., Sa, J., Smolentsev, G., Szlachetko, M., van Bokhoven, J. A., Dousse, J. C., Hoszowska, J., Kayser, Y., Jagodzinski, P., Bergamaschi, A., Schmitt, B., David, C. & Lücke, A. (2012). *Rev. Sci. Instrum.* **83**, 103105.

Uhlig, J., Doriese, W. B., Fowler, J. W., Swetz, D. S., Jaye, C., Fischer, D. A., Reintsema, C. D., Bennett, D. A., Vale, L. R., Mandal, U., O'Neil, G. C., Miaja-Avila, L., Joe, Y. I., El Nahhas, A., Fullagar, W., Parnefjord Gustafsson, F., Sundström, V., Kurunthu, D., Hilton, G. C., Schmidt, D. R. & Ullom, J. N. (2015). *J. Synchrotron Rad.* **22**, 766–775.

Zastrau, U., Brown, C. R. D., Döppner, T., Glenzer, S. H., Gregori, G., Lee, H. J., Marschner, H., Toleikis, S., Wehrhan, O. & Förster, E. (2012). *J. Instrum.* **7**, P09015.

Zhou, K.-J., Walters, A., Garcia-Fernandez, M., Rice, T., Hand, M., Nag, A., Li, J., Agrestini, S., Garland, P., Wang, H., Alcock, S., Nistea, I., Nutter, B., Rubies, N., Knap, G., Gaughran, M., Yuan, F., Chang, P., Emmins, J. & Howell, G. (2022). *J. Synchrotron Rad.* **29**, 563–580.

Zimmermann, P., Peredkov, S., Abdala, P. M., DeBeer, S., Tromp, M., Müller, C. & van Bokhoven, J. A. (2020). *Coord. Chem. Rev.* **423**, 213466.